iScience

CellPress
OPEN ACCESS

Article

Programmable VO_2 metasurface for terahertz wave beam steering

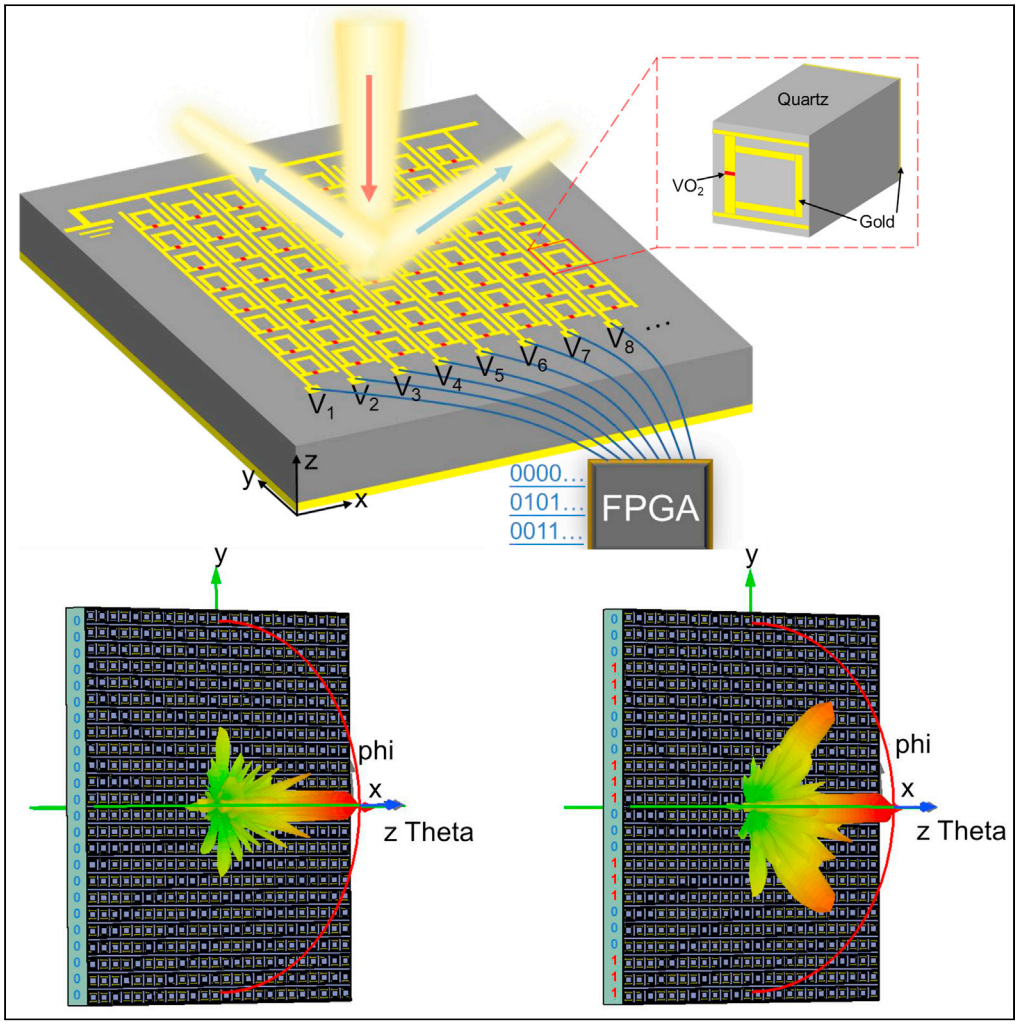

Daquan Yang, Weiguang Wang, Erpeng Lv, Haiming Wang, Bingchao Liu, Yanzhao Hou, Jinhui Chen

houyanzhao@bupt.edu.cn (Y.H.)
jimchen@xmu.edu.cn (J.-h.C.)

Highlights

The reversible phase-transition material VO_2 is integrated into the metasurface

Programmable VO_2 metasurfaces are proposed to achieve THz beam steering

Wide-angle beam scanning from −60° to +60° is realized in the digitalized metasurface

Yang et al., iScience 25, 104824
August 19, 2022
https://doi.org/10.1016/j.isci.2022.104824

iScience

CellPress
OPEN ACCESS

Article

Programmable VO_2 metasurface for terahertz wave beam steering

Daquan Yang,[1,2] Weiguang Wang,[1] Erpeng Lv,[1] Haiming Wang,[3] Bingchao Liu,[3] Yanzhao Hou,[1,4,*] and Jin-hui Chen[5,6,*]

SUMMARY

Programmable vanadium dioxide (VO_2) metasurface is proposed at THz frequencies. The insulating and metallic states of VO_2 can be switched via external electrical stimulation, resulting in the dynamical modulation of electromagnetic response. The voltages of different columns of the metasurface can be controlled by the field-programmable gate array, and thus the phase gradients are realized for THz beam steering. In 1-bit coding, we design periodic and nonperiodic 24 × 24 coding sequences, and achieve wide-angle beam scanning with the deflection angles from −60° to +60°. In 2-bit coding, we use two different meta-atoms to design 18 × 18 coding sequences. Compared with 1-bit coding, 2-bit coding has more degree of freedom to control the optical phase, and 3 dB diffraction efficiency is improved by generating a single deflection angle. The proposed programmable metasurfaces provide a promising platform for manipulating electromagnetic wave in 6G wireless communication.

INTRODUCTION

Terahertz (THz) wave, which is located between the infrared and microwave bands, has several unique characteristics such as extracting molecular spectral information, signal detection, and material characterization compared with mmWave bands (Ferguson and Zhang, 2002; Rappaport et al., 2019). Up to now, THz technology has already attracted significant attention in security checking, wireless communication, radar monitoring, biomedical applications, and other areas (Nagatsuma et al., 2016; Tonouchi, 2007; Heinz et al., 2015; Siegel, 2002, 2004; Zhang et al., 2014; Choi et al., 2011; Chan et al., 2007; Liu et al., 2007; Plusquellic et al., 2007). With the further expanding applications of THz technology, efficient functional devices and components are highly desirable. However, most of the natural materials cannot strongly respond to THz wave, which hampers the development of THz devices (Withayachumnankul and Abbott, 2009). As a subwavelength structure, the meta-atom can exhibit electrical polarization and magnetic polarization defined by the material and geometry (Meinzer et al., 2014). The metasurface can be formed by periodic arrays of meta-atoms, providing an ideal platform for the realization of THz functional devices (Zhang et al., 2008, 2013; Landy et al., 2008; Ben Mbarek et al., 2019; Wang et al., 2020; Wu et al., 2020; Rouhi et al., 2018; Shabanpour et al., 2020; Cong and Singh, 2020; Cong et al., 2018). Nevertheless, the properties of most metasurfaces are restricted by the fixed geometric parameters of meta-atoms. The dynamic functions such as beam scanning, frequency shifting, or amplitude modulation cannot be implemented on the basis of the mentioned metasurfaces. Therefore, hybrid metasurface combined with tunable materials such as graphene (Tamagnone et al., 2018; Wu et al., 2018; Cheng et al., 2016; Shi et al., 2015; Lu et al., 2021; Ghosh and Chaudhuri, 2018), liquid crystal (Song et al., 2017; Meng et al., 2019; Ji et al., 2020), and phase transition materials (Hashemi et al., 2016; Li et al., 2020c; Cen et al., 2019; Park et al., 2018; Leitis et al., 2020; Yin et al., 2017; Sreekanth et al., 2019) is considered as the promising approach to dynamically manipulating the response of THz wave.

Among the wide varieties of THz dynamic regulation devices, THz beam steering has drawn more attention in wireless communications. Until now, hybrid metasurfaces have been proposed to realize THz beam steering. For example, R. Singh et al. presented a spatiotemporal metasurface based on silicon to inhibit the backscattering and achieved 34.7° beam deflection for ultrafast beam scanning, which fulfilled the emerging demand for THz communication (Cong and Singh, 2020). Tamagnone et al. integrated graphene as an active element into metasurface, and the angular steering range reached 25° (Tamagnone et al., 2018). Wu et al. integrated liquid crystal material into the metasurface to achieve coding sequences with

[1]School of Information and Communication Engineering, Beijing University of Posts and Telecommunications, Beijing 100876, China

[2]State Key Laboratory of Information Photonics and Optical Communications, Beijing University of Posts and Telecommunications, Beijing 100876, China

[3]Lenovo Research, Beijing 100094, China

[4]National Engineering Laboratory for Mobile Network Technologies, Beijing University of Posts and Telecommunications, Beijing 100876, China

[5]Institute of Electromagnetics and Acoustics, Xiamen University, Xiamen 361005, China

[6]Lead contact

*Correspondence: houyanzhao@bupt.edu.cn (Y.H.), jimchen@xmu.edu.cn (J.-h.C.)

https://doi.org/10.1016/j.isci.2022.104824

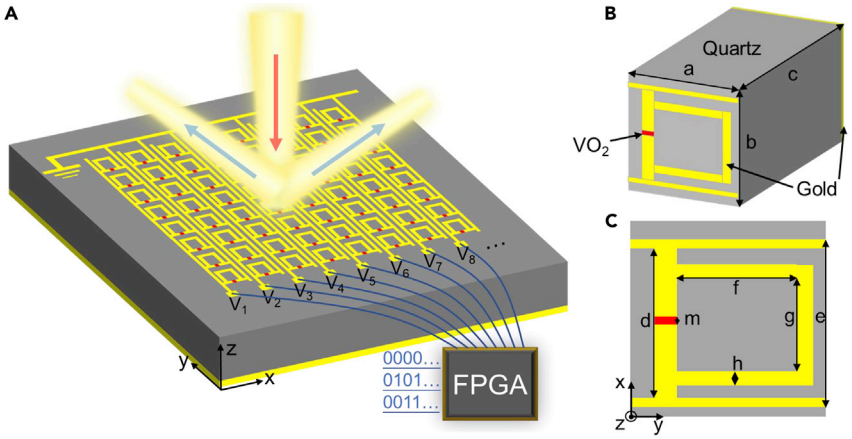

Figure 1. Schematic configuration of 1-bit programmable metasurface

(A) Schematic of beam steering by separately adjusting the voltage of each column controlled by the field-programmable gate array (FPGA).

(B) The meta-atom of the proposed 1-bit coding.

(C) The top view of the meta-atom.

a maximum deflection angle of 32° (Wu et al., 2020). However, it is difficult to achieve wide-angle scanning for these structures integrated with tunable materials. Wu et al. designed the hybrid coding metasurface to cover 360° beam deflection by utilizing the tunable chemical potential of graphene (Wu et al., 2018). Although the coverage angle is relatively large, it has only six main radiation directions. Therefore, it is still challenging to realize real time controlling the wide deflection angle of THz beam. Programmable metasurfaces have been demonstrated to be suitable for real-time control of electromagnetic wave (Ghorbani et al., 2021; Shabanpour et al., 2021a; Chen et al., 2022). Vanadium dioxide (VO_2) is a reversible phase-transition material triggered by thermal, optical, or electrical excitations, and it has advantages of the fast response and large modulation depth (Huang et al., 2020). The switch time of the phase transition can reach a scale of some femtoseconds at THz frequency, which can be much shorter than that of liquid crystals (Shabanpour et al., 2021b; Bai et al., 2019). Combined with the VO_2, metasurface is used to realize the dynamic regulation of THz wave such as frequency shifting and beam steering (Hashemi et al., 2016; Li et al., 2020b).

In this paper, we propose programmable VO_2 metasurfaces for manipulating terahertz electromagnetic wave. Two different VO_2 metasurfaces with 1-bit and 2-bit coding configurations are systematically studied. In 1-bit coding, the meta-atom achieves optical phase difference of π. In 2-bit coding, the two meta-atoms (type-A and type-B) are used to achieve phase difference of $\pi/2$. The above meta-atoms are controlled by the field-programmable gate array (FPGA), where all the meta-atoms in a column always have the same state. By adjusting coding sequences, the THz beam can be diffracted to different deflection angles. The results show that 1-bit programmable metasurface can achieve wide beam scanning between −60° and +60°. Since 2-bit programmable metasurface has more degree of freedom on phase control, 3 dB diffracting energy efficiency is improved by generating a single deflection angle. The designed devices show great potential for manipulating electromagnetic wave in THz regime.

DESIGN AND SIMULATION OF PROGRAMMABLE METASURFACE

1-bit programmable metasurface

The schematic of 1-bit programmable VO_2 metasurface is shown in Figure 1A, which consists of the meta-atom arrays, dielectric substrate, and reflecting metal film. In this design, low-loss quartz (thickness of 500 μm) is selected to reduce the absorption loss; gold (thickness of 0.2 μm) is implemented as the pattern and substrate. To dynamically control the electromagnetic response of the unit cell, the VO_2 patch (thickness of 0.2 μm) is embedded in meta-atoms, as marked with the red region in Figures 1B and 1C. By applying external voltage, it can cause the metal-insulator transition (MIT) of VO_2 in the metasurface. Note that the origin of MIT in VO_2 remains unclear, it may be caused by joule heat (Kumar et al., 2013; Li et al., 2016) or electric current (Wu et al., 2011; Shi and Chen, 2019). Each column of the structure is

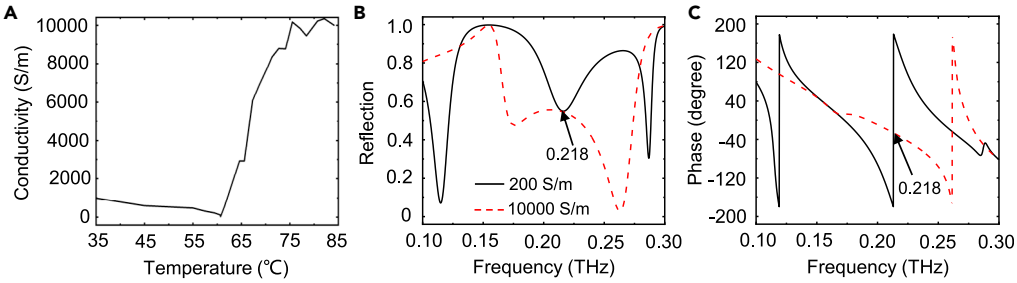

Figure 2. Tuanble VO_2 metasurface with phase transition

(A) The measured VO_2 conductivity under different temperatures.

(B) The simulated reflection amplitude of the meta-atom when VO_2 is in the insulating (conductivity of 200 S/m) and metallic states (conductivity of 10,000 S/m).

(C) The simulated phase of the meta-atom when VO_2 is in the insulating and metallic states.

independently controlled by the voltage (V_1, V_2, V_3, ...) from an FPGA. When one switch is toggled on, FPGA will input the corresponding electrical-voltage coding sequence. Consequently, the voltage distributions on the metasurface can be changed by toggling different triggers, thereby producing the required "0" and "1" states of the meta-atoms and achieving different phase gradient to manipulate THz waves.

VO_2 has two states, namely, the insulating state and the metallic state. The schematic structure of meta-atom is shown in Figure 1B. The geometric parameters of the meta-atom are as following: a = 320 μm, b = 320 μm, c = 500 μm, d = 240 μm, e = 270 μm, f = 175 μm, g = 120 μm, h = 35 μm, and m = 4 μm. When the VO_2 is in the metallic state, the metal arms are connected to form the ring circuit structure. When the VO_2 is in insulating state, the ring circuit structure is broken. Therefore, the equivalent circuit is completely different before and after the structural phase change. The electromagnetic response can be controlled through external excitation, and the proposed structure can obtain the phase gradients along the column separately, and then realize the purpose of THz beam steering.

As discussed above, the control of the metasurface is realized by exciting the VO_2 film. The VO_2 conductivity under different temperatures is measured as shown in Figure 2A. When the temperature is below 60°C, the conductivity of VO_2 film is <1,000 S/m, which means the insulating state. When the temperature is raised beyond 60°C, VO_2 film undergoes a structural phase transition and the conductivity also significantly increases. The film conductivity value is measured of ~10,000 S/m in metallic state after the end of the phase-transition process. According to the measured conductivity, the Drude model can be used to describe the dielectric properties of VO_2 at THz frequency (Li et al., 2020a; Wang et al., 2017; Liu et al., 2012). Therefore, the metasurface uses the great different conductivities between two states of VO_2 to realize beam steering.

The light diffractions in metasurface follow the generalized Snell's formula can be written as:

$$sin\theta_r - sin\theta_i = \frac{\lambda_0}{2\pi n_i}\frac{d\varphi}{dx} \quad \text{(Equation 1)}$$

where θ_r and θ_i represent the reflection angle and incident angle of THz wave, λ_0 is the operating wavelength and n_i is refraction index of the medium above the metasurface, and $d\varphi/dx$ corresponds to the phase gradient endowed by metasurface. Based on the geometric parameters of the metasurface, the formula calculates the deflection direction of the THz beam. Considering the light deflection into air under the normal incident THz wave, the formula can be simplified as:

$$sin\theta_r = \frac{\lambda_0}{2\pi}\frac{d\varphi}{dx} \quad \text{(Equation 2)}$$

And the radiation direction of the reflected THz beam can be calculated as:

$$\theta_r = arcsin\left(\frac{\lambda_0}{2\pi}\frac{d\varphi}{dx}\right) \quad \text{(Equation 3)}$$

The deflection direction of THz beam can be obtained by setting the appropriate phase gradient. In this design, the phase gradient is generated when the metallic and insulating elements have the same

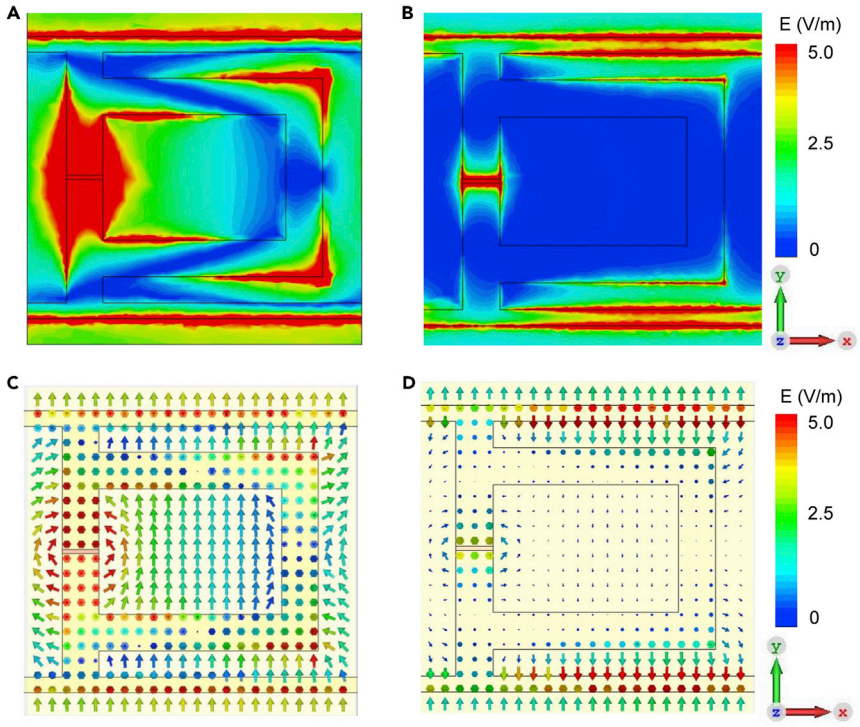

Figure 3. Electric field distributions in the metasurface unit

Electric field distributions in the top surface of the metasurface when VO_2 is in the (A) insulating and (B) metallic states The electric field vector distributions in the top surface of the metasurface when VO_2 is in the (C) insulating and (D) metallic states. The arrows indicate the field vectors.

reflection amplitude and phase difference of π. The simulations are performed by CST Microwave Studio to effectively investigate the electromagnetic responses of the metasurface. As shown in Figure 2C, the phase difference of meta-atom approaches π under the phase transition of VO_2 at 0.218 THz. The same reflection amplitude in Figure 2B ensures the accuracy of generalized Snell's law used in the beam steering. Note that the reflection amplitude can be increased by using the higher value of conductivity in the metallic state of the VO_2 (Shabanpour et al., 2020; Li et al., 2020c).

We first analyze the change of the field distributions before and after the VO_2 phase transition. The designed structure is illuminated by an incident plane wave; meanwhile, the electric field monitor is selected to observe the field distributions. Figures 3A and 3B show the electric field patterns before and after the phase transition of VO_2 at 0.218 THz. Before the phase transition, the VO_2 patch is in an insulating state and acts as a capacitor, this resonance circuit forms a split-ring resonator. It can be seen in Figure 3 that the free charges accumulate at the patch with a strong electric field intensity. When the VO_2 patch is in the metallic state, the metal arms are connected which results in a weaker electric field intensity. The VO_2 conductivity of metallic state is lower than that of gold, thus the accumulated charges cannot disappear completely. The electric field vector distributions before and after the phase transition of VO_2 are researched, as shown in Figures 3C and 3D. When the VO_2 is in the insulating state, the electric field vectors are concentrated on the VO_2 patch. When the VO_2 is in the metallic state, the electric field vectors are low and the distributions are relatively uniform. Therefore, the change of reflection phase before and after the phase transition of VO_2 is resulted from the change of capacitance in the circuit model.

Furthermore, to verify the effect of the VO_2 patch, the influence of the size and position of the VO_2 patch on the reflection amplitude and phase is investigated. Figure 4A and 4B show the changes of the reflection amplitude and phase when the offset position P of VO_2 patch varies from 0 μm to 20 μm. It is found that the offset position of VO_2 patch has little influence on the reflection amplitude and phase of meta-atom. Since the symmetrical structure is not sensitive to the polarization angle, the offset length is selected as 0 μm. When the width of VO_2 patch varies, the results are shown in Figures 4C and 4D. Before the phase

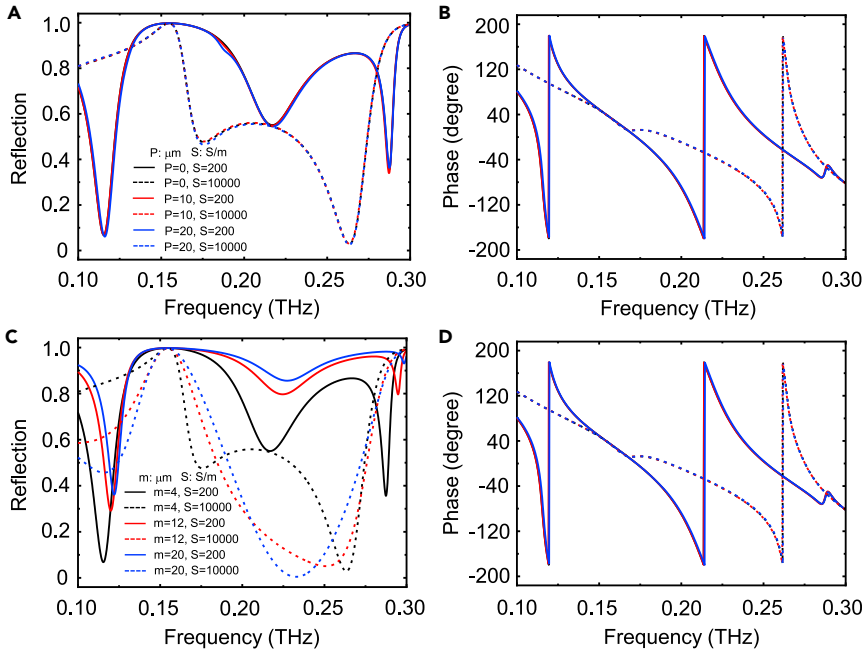

Figure 4. Meta-atom structural optimization for optical response

The reflection amplitude (A) and phase (B) curves of the meta-atom with different structural parameters (*P*) when VO_2 is in the metallic and insulating states. The parameter is defined as the offset position of the VO_2 patch relative to the center of the metal arm. The reflection amplitude (C) and phase (D) curves of the meta-atom with different VO_2 patch width (*m*) when VO_2 is in the metallic and insulating states.

transition, the reflection amplitude increases and the phase decreases with the increase of VO_2 patch width. When the phase transition is triggered, the variation tendency is opposite. The reason for this phenomenon is that the accumulated charge capacity under the insulating state is different. It can be seen that the volume of VO_2 patch has significant effect on the amplitude and phase of reflection. In order to achieve the best performance, the same reflection amplitude in the metallic and insulating states is required. When the optical phase difference is satisfied with π, metasurface can achieve beam deflection by generating optical phase gradient. Therefore, the VO_2 patch width is selected as 4 μm. The optimized geometric parameters are what we selected in the structural design.

In the analysis of Figure 2, the meta-atom has the same reflection amplitude and π phase difference in the insulating and metallic states, which are coded as "0" and "1". In order to realize the beam steering in far-field scattering pattern, meta-atoms should be symmetrically arranged in a spatial staggered manner to form a metasurface. The elements in the column are controlled by the same voltage. Therefore, the far-field radiation patterns of different encoded 24 × 24 metasurfaces are researched in detail, as shown in Figures 5A–5C. Figure 5A exhibits the reflection angle of all meta-atoms which are encoded as "0". Because the coding sequence "0000…" represents the insulating state, no phase gradient is generated between the columns; the metasurface mainly produces a reflected beam around in 0°. Then, the 1-bit coding is encoded with "000111…", as shown in Figure 5B. At 0.218 THz, two deflected beams are observed on −45°/+45°. Figure 5C gives the 1-bit coding which is encoded with "00001111…" and the two beam directions are −30°/+30° at 0.218 THz. In addition to the target beam deflection, metasurface also generates zero-order diffraction, which can be suppressed by introducing supercell structures (Shabanpour et al., 2020). Moreover, the diffraction characteristics of the far field are calculated by the classical Fraunhofer diffraction formula. As shown in Figure 5D, when the elements are completely coded as "0000…", the reflected beam is focused on 0°. In Figures 5E and 5F, two deflected beams of the coding sequence "000111…" and "00001111…" are observed on −44.7°/+44.7° and −31.5°/+31.5°, respectively.

The periodic design means that the number of columns is divisible by the number of a single coding period. Since the number of periodic coding sequence is finite, beam scanning requires more coding sequences to improve the accuracy of beam directions. Therefore, the nonperiodic design, *i.e.* the total columns are not

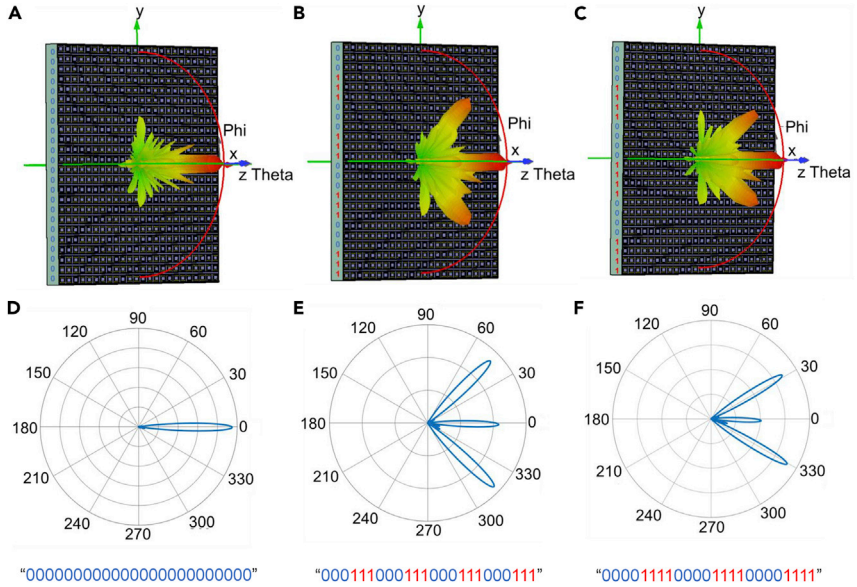

Figure 5. Simulated and calculated far-field patterns of the designed 24 × 24 metasurface with different periodic coding sequences of "0000…"

(A–F) (A and D), "000111…" (B and E), and "00001111…" (C and F) at 0.218 THz.

divisible by a single coding period, is proposed to realize the deflection of beams. As shown in Figures 6A–6C), when the metasurface is coded as "000011111…", "0001111…", and "00111…", two deflected beams are observed on −28°/+28°, −35°/+35°, and −60°/+60°, respectively. Note that the nonperiodic coding sequence affects the phase gradient distribution on the metasurface, resulting in asymmetric beams. In Figures 6D–6F, two deflected beams of the above coding sequences are observed on −28.4°/+28.4°, −37.1°/+37.1°, and −58.9°/+58.9° by numerical calculation. The simulations coincide with theoretical results. Table 1 shows the comparisons of the different metasurfaces for THz beam steering. In this work, the 1-bit programmable metasurface can achieve tunable and wide beam scanning between −60° and +60°, which provides a promising platform for beam steering at 6G frequencies.

2-bit programmable metasurface

The concept of the programmable metasurface can be extended from 1-bit to 2-bit or higher coding (Cui et al., 2014). In 2-bit coding, four states with different electromagnetic responses are required to mimic the "00", "01", "10", and "11" coding. The two states of 1-bit programmable metasurface need to achieve π phase difference, then the four states of 2-bit programmable metasurface are required to achieve $\pi/2$ phase difference, such as 0, $\pi/2$, π, and $3\pi/2$. Therefore, 2-bit coding has more degree of freedom to manipulate electromagnetic waves compared with 1-bit coding.

To realize 2-bit coding, we design two meta-atoms labeled type-A and type-B with different geometries, as shown in Figure 7A. It shows that the 2-bit programmable VO_2 metasurface is controlled by FPGA, in which type-A and type-B are in a staggered arrangement. The 2-bit programmable metasurface also consists of the meta-atom arrays, the dielectric substrate, and back metal film. The geometric parameters of type-A (type-B) are listed: a = 300 μm, b = 300 μm, c = 500 μm, d = 240 (150) μm, e = 270 (170) μm, f = 175 (110) μm, g = 115 (90) μm, h = 35 (15) μm, and m = 4 (3) μm. Each meta-atom (A or B) can be electrically tuned between insulting and metallic states. The deflection function of the THz beam can be achieved when the condition of phase gradient is satisfied. The 2-bit coding can improve the accuracy of beam directions. As shown in Figure 7B, the amplitudes of the two types before and after phase transition are 0.5. In Figure 7C, the optical phase of type-A has $5\pi/6$ and $11\pi/6$, and the phase of type-B has $4\pi/3$ and $\pi/3$. Therefore, both of meta-atoms can satisfy the $\pi/2$ phase difference. We use "00" ("01") for the insulating (metallic) state of type-A and "10" ("11") for the insulating (metallic) state of type-B. Similar to the 1-bit programmable metasurface, each column has the same element type in the 2-bit programmable metasurface. By controlling each column with FPGA, the conductivity of each column VO_2 can be changed, thus realizing the manipulation of the deflection angle.

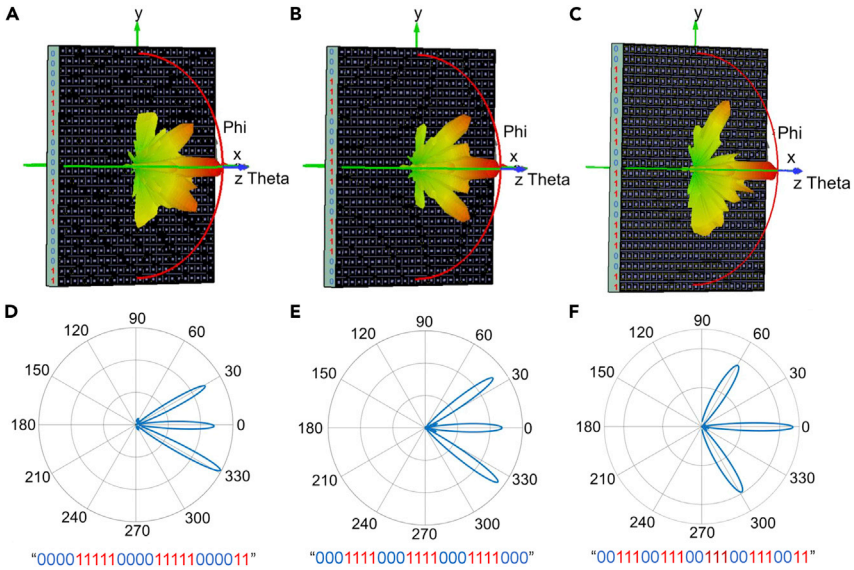

Figure 6. Simulated and calculated far-field patterns of the designed 24 × 24 metasurface with different nonperiodic coding sequences of "000011111…"

(A–F) (A and D), ''0001111…'' (B and E), and ''00111…'' (C and F), respectively at 0.218 THz.

Based on type-A and type-B, the 18 × 18 metasurface with different 2-bit coding sequences has been designed. We remark that "0", "1", "2", and "3" as the "00", "01", "10", and "'11". It can be seen that the metasurface with coding sequences in Figures 8A–8D has main beam directions of +20°, +30°, +40°, and +50° at 0.22 THz. Correspondingly, the numerical results also show that the beam deflections of +20.1°, +31.5°, +41.8°, and +50.0° are generated in Figures 8E–8H. The 2-bit coding can achieve a single deflection angle. Thus, 3 dB diffraction energy efficiency is improved. When the above coding sequences in Figure 8 are inverted, such as "0123" to "3210", it can achieve a symmetrical beam deflection between −20° and −50°. To prove the flexibility of 2-bit encoding, we design other coding sequences in Figure 9. It can be seen that the metasurface with 2-bit coding sequences in Figures 9A–9D achieves main beam directions of −20°, −30°, −40°, and −50° at 0.22 THz. The calculated results show that the beam deflections of −22.1°, −31.7°, −42.1°, and −53.1° are generated in Figures 9E–9H. Therefore, the simulations coincide with theoretical results, and the same beam deflection can be achieved with different coding sequences. 2-bit programmable metasurface has higher freedom on phase and more flexible coding sequences.

Conclusions

In summary, we report 1-bit and 2-bit programmable VO_2 metasurfaces which realize phase difference of π and $\pi/2$, respectively. Combining with the FPGA, metasurface can be applied to change the direction of beam deflection by dynamically configuring the coding sequences in real-time. The 1-bit coding can achieve wide deflection angles between −60° and +60° by generating two symmetrical deflection angles. The 2-bit programmable metasurface has higher freedom of control on phase and achieves a single deflection angle with 3 dB diffraction efficiency improvement compared with 1-bit programmable metasurface.

Table 1. Comparisons of different metasurfaces for THz beam steering

Material	Tuning methods	Performance
Silicon (Cong and Singh, 2020)	Femtosecond laser pulses	34.7° deflection angle Non-tunable
Graphene (Tamagnone et al., 2018)	Voltage controlled by Arduino	25° deflection angle Tunable
Graphene (Wu et al., 2018)	Changing the graphene chemical potential	6 fixed directions cover 360° Tunable but Discontinuous
Liquid crystal (Wu et al., 2020)	Voltage controlled by FPGA	32° deflection angle Tunable and Digital
Vanadium dioxide (This work)	Voltage controlled by FPGA	± 60° deflection angle Tunable and Digital

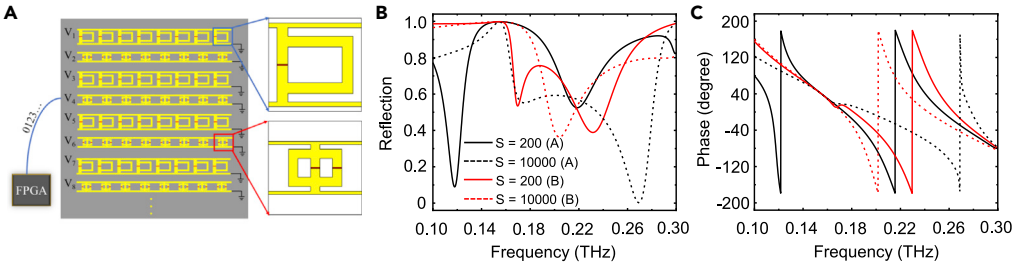

Figure 7. The 2-bit programmable metasurface

(A) The schematic view of 2-bit programmable metasurface. Simulated reflection amplitude (B) and phase (C) of the meta-atoms when VO_2 is in the insulating and metallic states.

The simulation results coincide with theoretical results. This work offers a promising method of dynamic beam deflection at 6G frequencies and enables the broad adoption of wireless communication.

Limitations of the study

In this study, we propose programmable VO_2 metasurfaces which can dynamically control the deflection angle of the THz beam. While, we cannot conduct the device fabrications and performance measurement due to the lack of experimental conditions. Based on the previous work (Shabanpour et al., 2020; Chen et al., 2022), the meta-atom structures can be possibly fabricated as follows: First, a layer of VO_2 (0.2 μm thick) is deposited on the quartz substrate (500 μm thick) by reactive magnetron sputtering. Next, the pattern of VO_2 patch is formed by the lithography and reactive ion etching. Finally, a layer of gold (0.2 μm thick) is deposited on the bottom of quartz substrate, and the gold pattern is fabricated on the top surface of quartz by the second lithography and metallic deposition. The optical response of as fabricated device can be characterized by the commercial THz system. In the future study, we may seek for the cooperation for the device fabrication and measurement.

STAR★METHODS

Detailed methods are provided in the online version of this paper and include the following:

- KEY RESOURCES TABLE
- RESOURCE AVAILABILITY
  - Lead contact

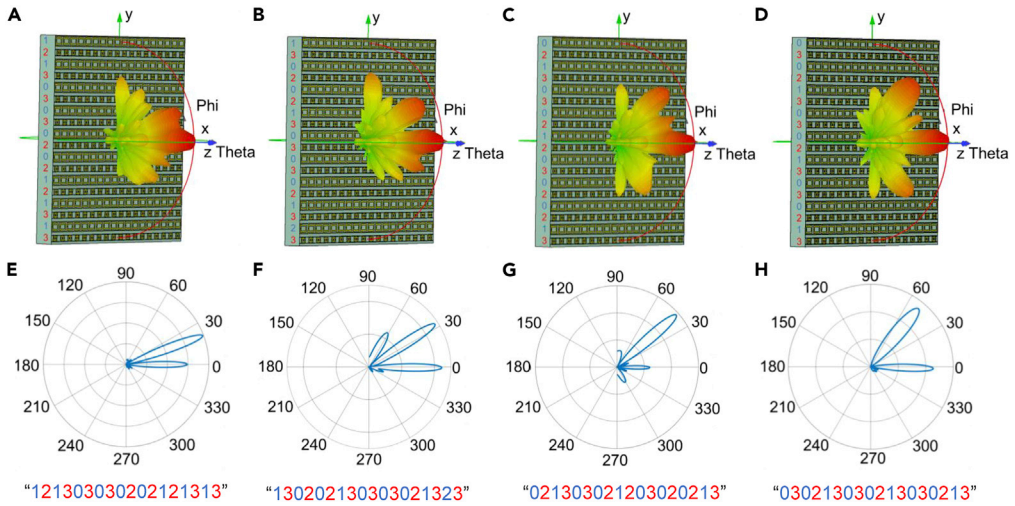

Figure 8. Simulated and calculated far-field patterns of the designed 18 × 18 metasurface with different 2-bit coding sequences of "121303030202121313"

(A–H) (A and E), "130202130303021213" (B and F), "021303021203020213" (C and G), and "030213030213030213" (D and H), respectively at 0.22 THz.

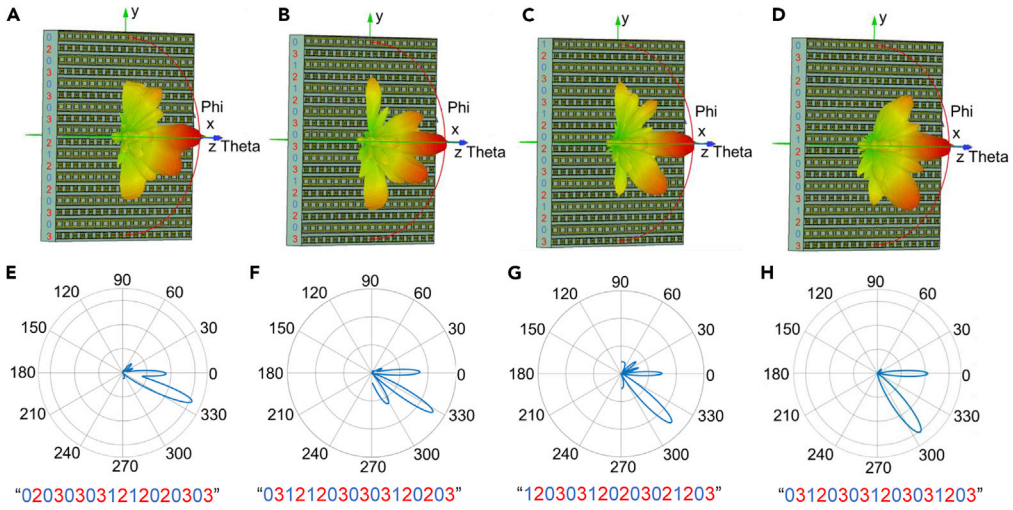

Figure 9. Simulated and calculated far-field patterns of the designed 18 × 18 metasurface with different 2-bit coding sequences of "020303031212020303"

(A–H) (A and E), "031212030303120203" (B and F), "120303120203021203" (C and G), and "031203031203031203" (D and H), respectively at 0.22 THz.

- Materials availability
- Data and code availability

- EXPERIMENTAL MODEL AND SUBJECT DETAILS
- METHOD DETAILS
- QUANTITATION AND STATISTICAL ANALYSIS
- ADDITIONAL RESOURCES

ACKNOWLEDGMENTS

This work is supported by National Natural Science Foundation of China (11974058, 62005231); Beijing Nova Program (Z201100006820125) from Beijing Municipal Science and Technology Commission; Beijing Natural Science Foundation (Z210004); and State Key Laboratory of Information Photonics and Optical Communications (IPOC2021ZT01), BUPT, China.

AUTHOR CONTRIBUTIONS

All the authors have contributed greatly. Conceptualization: J.C. and D.Y.; Design: D.Y. and W.W.; Writing: W.W. and E.L.; Editing: J.C. and D.Y.; Simulation and Calculation: W.W. and E.L.; Funding Acquisition: J.C. and D.Y.; Supervision: H.W., B.L. and Y.H.

DECLARATION OF INTERESTS

The authors declare no conflicts of interest.

Received: March 28, 2022
Revised: June 29, 2022
Accepted: July 19, 2022
Published: August 19, 2022

REFERENCES

Bai, J., Zhang, S., Fan, F., Wang, S., Sun, X., Miao, Y., and Chang, S. (2019). Tunable broadband THz absorber using vanadium dioxide metamaterials. Opt Commun. *452*, 292–295. https://doi.org/10.1016/j.optcom.2019.07.057.

Ben Mbarek, S., Tennich, A., and Choubani, F. (2019). Analytical modeling of cross metallic metasurfaces absorption for terahertz band. J. Electromagn. Waves Appl. *33*, 1343–1353. https://doi.org/10.1080/09205071.2019.1608317.

Cen, G., Deng, H., Cheng, L., Zhou, S., and Liao, S. (2019). Terahertz (THz) metasurface switch by phase change medium. IEEE MTT-S International Wireless Symposium, 1–3. https://doi.org/10.1109/IEEEIWS.2019.8803956.

Chan, W.L., Deibel, J., and Mittleman, D.M. (2007). Imaging with terahertz radiation. Rep. Prog. Phys. *70*, 1325–1379. https://doi.org/10.1088/0034-4885/70/8/R02.

Chen, B., Wu, J., Li, W., Zhang, C., Fan, K., Xue, Q., Chi, Y., Wen, Q., Jin, B., Chen, J., et al. (2022). Programmable terahertz metamaterials with non-volatile memory. Laser Photon. Rev. *16*, 2100472. https://doi.org/10.1002/lpor.202100472.

Cheng, X., Yao, Y., Qu, S., Wu, Y., Yu, J., and Chen, X. (2016). Circular beam-reconfigurable antenna base on graphene-metal hybrid. Electron. Lett. *52*, 494–496. https://doi.org/10.1049/el.2015.4435.

Choi, M., Lee, S.H., Kim, Y., Kang, S.B., Shin, J., Kwak, M.H., Kang, K.Y., Lee, Y.H., Park, N., and Min, B. (2011). A terahertz metamaterial with unnaturally high refractive index. Nature *470*, 369–373. https://doi.org/10.1038/nature09776.

Cong, L., and Singh, R. (2020). Spatiotemporal dielectric metasurfaces for unidirectional propagation and reconfigurable steering of terahertz beams. Adv. Mater. *32*, 2001418. https://doi.org/10.1002/adma.202001418.

Cong, L., Srivastava, Y.K., Zhang, H., Zhang, X., Han, J., and Singh, R. (2018). All-optical active THz metasurfaces for ultrafast polarization switching and dynamic beam splitting. Light Sci. Appl. *7*, 28. https://doi.org/10.1038/s41377-018-0024-y.

Cui, T.J., Qi, M.Q., Wan, X., Zhao, J., and Cheng, Q. (2014). Coding metamaterials, digital metamaterials and programmable metamaterials. Light Sci. Appl. *3*, e218. https://doi.org/10.48550/10.1038/lsa.2014.99.

Ferguson, B., and Zhang, X.C. (2002). Materials for terahertz science and technology. Nat. Mater. *1*, 26–33. https://doi.org/10.1038/nmat708.

Ghorbani, F., Beyraghi, S., Shabanpour, J., Oraizi, H., Soleimani, H., and Soleimani, M. (2021). Deep neural network-based automatic metasurface design with a wide frequency range. Sci. Rep. *11*, 7102. https://doi.org/10.1038/s41598-021-86588-2.

Ghosh, J., and Chaudhuri, S.R.B. (2018). Design of graphene metasurface to mitigate mutual coupling in monopole antenna at lower THz frequency. ICMAP *1–2*. https://doi.org/10.1109/ICMAP.2018.8354584.

Hashemi, M.R.M., Yang, S.H., Wang, T., Sepúlveda, N., and Jarrahi, M. (2016). Electronically-controlled beam-steering through vanadium dioxide metasurfaces. Sci. Rep. *6*, 35439–35448. https://doi.org/10.1038/srep35439.

Heinz, E., May, T., Born, D., Zieger, G., Anders, S., Zakosarenko, V., Meyer, H.G., and Schäffel, C. (2015). Passive 350 GHz video imaging systems for security applications. J. Infrared, Millim. Terahertz Waves *36*, 879–895. https://doi.org/10.1007/s10762-015-0170-8.

Huang, J., Li, J., Yang, Y., Li, J., Li, J., Zhang, Y., and Yao, J. (2020). Active controllable dual broadband terahertz absorber based on hybrid metamaterials with vanadium dioxide. Opt Express *28*, 7018–7027. https://doi.org/10.1364/OE.387156.

Ji, Y.Y., Fan, F., Zhang, X., Cheng, J.R., and Chang, S. (2020). Active terahertz anisotropy and dispersion engineering based on dual-frequency liquid crystal and dielectric metasurface. J. Lightwave Technol. *38*, 4030–4036. https://doi.org/10.1109/JLT.2020.2985667.

Kumar, S., Pickett, M.D., Strachan, J.P., Gibson, G., Nishi, Y., and Williams, R.S. (2013). Local temperature redistribution and structural transition during joule-heating-driven conductance switching in VO_2. Adv. Mater. *25*, 6128–6132. https://doi.org/10.1002/adma.201302046.

Landy, N.I., Sajuyigbe, S., Mock, J.J., Smith, D.R., and Padilla, W.J. (2008). Perfect metamaterial absorber. Phys. Rev. Lett. *100*, 207402. https://doi.org/10.1103/PhysRevLett.100.207402.

Leitis, A., Heßler, A., Wahl, S., Wuttig, M., Taubner, T., Tittl, A., and Altug, H. (2020). All-dielectric programmable huygens' metasurfaces. Adv. Funct. Mater. *30*, 1910259. https://doi.org/10.1002/adfm.201910259.

Li, D., Sharma, A.A., Gala, D.K., Shukla, N., Paik, H., Datta, S., Schlom, D.G., Bain, J.A., and Skowronski, M. (2016). Joule heating-induced metal–insulator transition in epitaxial VO_2/TiO_2 devices. ACS Appl. Mater. Interfaces *8*, 12908–12914. https://doi.org/10.1021/acsami.6b03501.

Li, H., Xu, W., Cui, Q., Wang, Y., and Yu, J. (2020a). Theoretical design of a reconfigurable broadband integrated metamaterial terahertz device. Opt Express *28*, 40060–40074. https://doi.org/10.1364/OE.414961.

Li, J.H., Zhang, Y.T., Li, J.N., Li, J., Li, J.T., Zheng, C.L., Yang, Y., Huang, J., Ma, Z.Z., Ma, C.Q., et al.; The Institute of Laser and Opto-electronics, School of Precision Instrument and Opto-Electronics Engineering, Tianjin University, Tianjin 300072, China; Key Laboratory of the Ministry of Education on Optoelectronic Information Technology, Tianjin University, Tianjin 300072, China (2020b). Terahertz coding metasurface based vanadium dioxide. Acta Phys. Sin. *69*, 228101. https://doi.org/10.7498/aps.69.20200891.

Li, J.S., Li, S.H., and Yao, J.Q. (2020c). Actively tunable terahertz coding metasurfaces. Opt Commun. *461*, 125186. https://doi.org/10.1016/j.optcom.2019.125186.

Liu, H.B., Zhong, H., Karpowicz, N., Chen, Y., and Zhang, X.C. (2007). Terahertz spectroscopy and imaging for defense and security applications. Proc. IEEE *95*, 1514–1527. https://doi.org/10.1088/0034-4885/70/8/R02.

Liu, M., Hwang, H.Y., Tao, H., Strikwerda, A.C., Fan, K., Keiser, G.R., Sternbach, A.J., West, K.G., Kittiwatanakul, S., Lu, J., et al. (2012). Terahertz-field-induced insulator-to-metal transition in vanadium dioxide metamaterial. Nature *487*, 345–348. https://doi.org/10.1038/nature11231.

Lu, Y., Wang, C., Zhao, S., and Wen, Y. (2021). Magnetically tunable graphene-based terahertz metasurface. Front. Phys. *8*, 661. https://doi.org/10.3389/fphy.2020.622839.

Meinzer, N., Barnes, W.L., and Hooper, I.R. (2014). Plasmonic meta-atoms and metasurfaces. Nat. Photonics *8*, 889–898. https://doi.org/10.1038/nphoton.2014.247.

Meng, X., Nekovee, M., and Wu, D. (2019). Reconfigurable liquid crystal reflectarray metasurface for THz communications. In Antennas and Propagation Conference (IET), pp. 1–6. https://doi.org/10.48550/arXiv.1908.02736.

Nagatsuma, T., Ducournau, G., and Renaud, C.C. (2016). Advances in terahertz communications accelerated by photonics. Nat. Photonics *10*, 371–379. https://doi.org/10.1038/nphoton.2016.65.

Park, D.J., Shin, J.H., Park, K.H., and Ryu, H.C. (2018). Electrically controllable THz asymmetric split-loop resonator with an outer square loop based on VO_2. Opt Express *26*, 17397–17406. https://doi.org/10.1364/OE.26.017397.

Plusquellic, D.F., Siegrist, K., Heilweil, E.J., and Esenturk, O. (2007). Applications of terahertz spectroscopy in biosystems. ChemPhysChem *8*, 2412–2431. https://doi.org/10.1016/j.dit.2013.03.009.

Rappaport, T.S., Xing, Y., Kanhere, O., Ju, S., Madanayake, A., Mandal, S., Alkhateeb, A., and Trichopoulos, G.C. (2019). Wireless communications and applications above 100 GHz: opportunities and challenges for 6G and beyond. IEEE Access *7*, 78729–78757. https://doi.org/10.1109/ACCESS.2019.2921522.

Rouhi, K., Rajabalipanah, H., and Abdolali, A. (2018). Real-time and broadband terahertz wave scattering manipulation via polarization-insensitive conformal graphene-based coding metasurfaces. Ann. Phys. 1700310. https://doi.org/10.1002/andp.201700310.

Shabanpour, J., Beyraghi, S., and Cheldavi, A. (2020). Ultrafast reprogrammable multifunctional vanadium-dioxide-assisted metasurface for dynamic THz wavefront engineering. Sci. Rep. *10*, 8950–9014. https://doi.org/10.1038/s41598- 020-65533-9.

Shabanpour, J., Beyraghi, S., Ghorbani, F., and Oraizi, H. (2021a). Implementation of conformal digital metasurfaces for THz polarimetric sensing. OSA Continuum *4*, 1372–1380. https://doi.org/10.1364/OSAC.421643.

Shabanpour, J., Sedaghat, M., Nayyeri, V., Oraizi, H., and Ramahi, O.M. (2021b). Real-time multi-functional near-infrared wave manipulation with a 3-bit liquid crystal based coding metasurface. Opt Express *29*, 14525–14535. https://doi.org/10.1364/OE.420972.

Shi, S.F., Zeng, B., Han, H.L., Hong, X., Tsai, H.Z., Jung, H.S., Zettl, A., Crommie, M.F., and Wang, F. (2015). Optimizing broadband terahertz modulation with hybrid graphene/metasurface structures. Nano Lett. *15*, 372–377. https://doi.org/10.1021/nl503670d.

Shi, Y., and Chen, L.Q. (2019). Current-driven insulator-to-metal transition in strongly correlated VO_2. Phys. Rev. Appl. *11*, 014059. https://doi.org/10.1103/PhysRevApplied.11.014059.

Siegel, P.H. (2002). Terahertz technology. IEEE Trans. Microw. Theory Tech. *50*, 910–928. https://doi.org/10.1109/22.989974.

Siegel, P.H. (2004). Terahertz technology in biology and medicine. IEEE Trans. Microw. Theory Tech. *52*, 2438–2447. https://doi.org/10.1109/TMTT.2004.835916.

Song, Q.H., Zhu, W.M., Wu, P.C., Zhang, W., Wu, Q.Y.S., Teng, J.H., Shen, Z.X., Chong, P.H.J., Liang, Q.X., Yang, Z.C., et al. (2017). Liquid-metal-based metasurface for terahertz absorption material: frequency-agile and wide-angle. Apl. Mater. *5*, 066103. https://doi.org/10.1063/1.4985288.

Sreekanth, K.V., Ouyang, Q., Sreejith, S., Zeng, S., Lishu, W., Ilker, E., Dong, W., ElKabbash, M., Ting, Y., Lim, C.T., et al. (2019). Phase-change material-based low-loss visible-frequency hyperbolic metamaterials for ultrasensitive label-free biosensing. Adv. Opt. Mater. *7*, 1900081. https://doi.org/10.1002/adom.201900081.

Tamagnone, M., Capdevila, S., Lombardo, A., Wu, J., Centeno, A., Zurutuza, A., Ionescu, A.M., Ferrari, A.C., and Mosig, J.R. (2018). Graphene reflectarray metasurface for terahertz beam steering and phase modulation. Preprint at arXiv. https://doi.org/10.48550/arXiv.1806.02202.

Tonouchi, M. (2007). Cutting-edge terahertz technology. Nat. Photonics *1*, 97–105. https://doi.org/10.1038/nphoton.2007.3.

Wang, L., Lan, F., Zhang, Y., Liang, S., Liu, W., Yang, Z., Meng, L., Shi, Z., Yin, J., Song, T., et al. (2020). A fractional phase-coding strategy for terahertz beam patterning on digital metasurfaces. Opt. Express *28*, 6395–6407. https://doi.org/10.1364/OE.385691.

Wang, S., Kang, L., and Werner, D.H. (2017). Hybrid resonators and highly tunable terahertz metamaterials enabled by vanadium dioxide (VO_2). Sci. Rep. *7*, 4326. https://doi.org/10.1038/s41598-017-04692-8.

Withayachumnankul, W., and Abbott, D. (2009). Metamaterials in the terahertz regime. IEEE Photonics J. *1*, 99–118. https://doi.org/10.1109/JPHOT.2009.2026288.

Wu, B., Hu, Y., Zhao, Y.T., Lu, W.B., and Zhang, W. (2018). Large angle beam steering THz antenna using active frequency selective surface based on hybrid graphene-gold structure. Opt Express *26*, 15353–15361. https://doi.org/10.1364/OE.26.015353.

Wu, B., Zimmers, A., Aubin, H., Ghosh, R., Liu, Y., and Lopez, R. (2011). Electric field-driven phase transition in vanadium dioxide. Phys. Rev. B *84*, 241410. https://doi.org/10.1103/PhysRevB.84.241410.

Wu, J., Shen, Z., Ge, S., Chen, B., Shen, Z., Wang, T., Zhang, C., Hu, W., Fan, K., Padilla, W., et al. (2020). Liquid crystal programmable metasurface for terahertz beam steering. Appl. Phys. Lett. *116*, 131104. https://doi.org/10.1063/1.5144858.

Yin, X., Steinle, T., Huang, L., Taubner, T., Wuttig, M., Zentgraf, T., and Giessen, H. (2017). Beam switching and bifocal zoom lensing using active plasmonic metasurfaces. Light Sci. Appl. *6*, e17016. https://doi.org/10.1038/lsa.2017.16.

Zhang, B., Pi, Y., and Li, J. (2014). Terahertz imaging radar with inverse aperture synthesis techniques: system structure, signal processing, and experiment results. IEEE Sens. J. *15*, 290–299. https://doi.org/10.1109/JSEN.2014.2342495.

Zhang, S., Genov, D.A., Wang, Y., Liu, M., and Zhang, X. (2008). Plasmon-induced transparency in metamaterials. Phys. Rev. Lett. *101*, 047401. https://doi.org/10.1103/PhysRevLett.101.047401.

Zhang, X., Tian, Z., Yue, W., Gu, J., Zhang, S., Han, J., and Zhang, W. (2013). Broadband terahertz wave deflection based on c-shape complex metamaterials with phase discontinuities. Adv. Mater. *25*, 4567–4572. https://doi.org/10.1002/adma.201204850.

STAR★METHODS

KEY RESOURCES TABLE

REAGENT or RESOURCE	SOURCE	IDENTIFIER
Software and algorithms		
CST	CST China Co., LTD.	https://www.cst-china.cn
MATLAB	MathWorks Co., LTD.	https://www.mathworks.com/products/matlab.html

RESOURCE AVAILABILITY

Lead contact

Further information and requests for resources and reagents should be directed to and will be fulfilled by the lead contact, Jin-hui Chen (jimchen@xmu.edu.cn).

Materials availability

This study did not generate new unique reagents.

Data and code availability

- Data reported in this paper will be shared by the lead contact upon request.
- This paper does not report original codes.
- Any additional information required to reanalyze the data reported in this paper is available from the lead contact upon request.

EXPERIMENTAL MODEL AND SUBJECT DETAILS

The CST Microwave Studio software has been employed to analyze the far-field patterns of the proposed programmable VO_2 metasurfaces. In these numerical simulations, the propagation direction of incident wave is set to be perpendicular to the x-y plane where the programmable VO_2 metasurface. The conductivity of VO_2 before and after phase transformation is 200 S/m and 10,000 S/m.

METHOD DETAILS

The simulation is conducted with the CST Microwave Studio software. The boundary conditions in the x and y directions are open, and the boundary conditions in the z direction are open (add space).

QUANTITATION AND STATISTICAL ANALYSIS

The simulation data is produced by CST Microwave Studio software. Figures shown in the main text were produced by Origin and Microsoft PowerPoint from the raw data.

ADDITIONAL RESOURCES

Any additional information about the simulation and data reported in this paper is available from the lead contact on request.